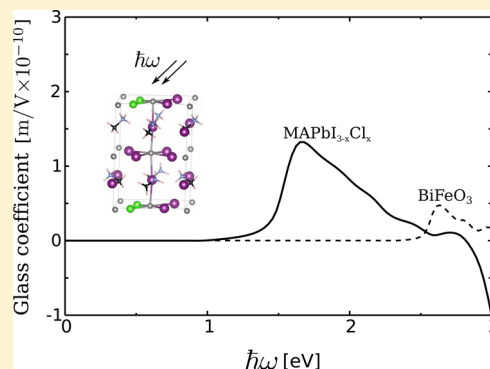


First-Principles Calculation of the Bulk Photovoltaic Effect in $\text{CH}_3\text{NH}_3\text{PbI}_3$ and $\text{CH}_3\text{NH}_3\text{PbI}_{3-x}\text{Cl}_x$

Fan Zheng, Hiroyuki Takenaka, Fenggong Wang, Nathan Z. Koocher, and Andrew M. Rappe*

The Makineni Theoretical Laboratories, Department of Chemistry, University of Pennsylvania, Philadelphia, Pennsylvania 19104-6323, United States

ABSTRACT: Hybrid halide perovskites exhibit nearly 20% power conversion efficiency, but the origin of their high efficiency is still unknown. Here, we compute the shift current, a dominant mechanism of the bulk photovoltaic (PV) effect for ferroelectric photovoltaics, in $\text{CH}_3\text{NH}_3\text{PbI}_3$ and $\text{CH}_3\text{NH}_3\text{PbI}_{3-x}\text{Cl}_x$ from first-principles. We find that these materials give approximately three times larger shift current PV response to near-IR and visible light than the prototypical ferroelectric photovoltaic BiFeO_3 . The molecular orientations of CH_3NH_3^+ can strongly affect the corresponding PbI_3 inorganic frame so as to alter the magnitude of the shift current response. Specifically, configurations with dipole moments aligned in parallel distort the inorganic PbI_3 frame more significantly than configurations with near-net-zero dipole, yielding a larger shift current response. Furthermore, we explore the effect of Cl substitution on shift current and find that Cl substitution at the equatorial site induces a larger response than does substitution at the apical site.



The power conversion efficiency of hybrid halide perovskites has almost doubled from 9.7%¹ to 19.3%² within 2 years. This attracts a great deal of interest in understanding the mechanism of its photovoltaic (PV) effect and in designing and optimizing the materials. Different synthetic methods and cell architectures can affect the final efficiency, implying that various PV mechanisms may contribute to the PV current.³ Particularly, the doping of Cl into $\text{CH}_3\text{NH}_3\text{PbI}_3$ (methylammonium lead iodide, MAPbI) increases the diffusion length of excited carriers by nearly one order of magnitude.⁴ Significant current effort focuses on understanding the underlying reason for this high PV efficiency. Both experimental measurements and theoretical calculations show that MAPbI and related materials, such as $\text{NH}_2\text{CHNH}_2\text{PbI}_3$ (formamidinium lead iodide, FAPbI), $\text{MAPbI}_{3-x}\text{Cl}_x$ (MAPbICl), $\text{MAPb}_x\text{Sn}_{1-x}\text{I}$ (MAPbSnI), and $\text{MAPbI}_{3-x}\text{Br}_x$ (MAPbIBr), have band gaps in the range of 1.1–2.1 eV in the visible light region.^{5–12} Their optical absorption strength is comparable to other classic semiconductors such as GaAs, InP, and CdTe.^{7,13–15} These materials also show relatively high and balanced electron and hole mobility and very fast electron–hole pair generation.^{16–18} In addition, the carrier diffusion length is more than 1 μm , implying a low concentration of deep defects.^{4,19–21} The source of their high power conversion efficiency, however, is still not clear.

Shift current has been proven to be a main mechanism of the bulk photovoltaic effect (BPVE) in ferroelectric oxides such as BaTiO_3 , PbTiO_3 , and BiFeO_3 .^{22–25} Single-phase noncentrosymmetric materials are able to generate DC current under uniform illumination. Shift current relies on

ballistic quantum coherent carriers; therefore, it can provide above-band-gap open-circuit photovoltage. MAPbI and related materials share similar perovskite structures with ferroelectric oxides. The tetragonal phase of MAPbI was found to have ferroelectric response at room temperature.¹¹ Various I/V hysteresis measurements suggest that the current is related to the ferroelectric response.^{26–30} In particular, the large measured open-circuit voltage allows for the possibility that the BPVE could make a big contribution to the photovoltage as the BPVE can generate a photovoltage that is above a material's band gap. Therefore, studying the BPVE of MAPbI-based materials is important in terms of elucidating the underlying mechanism of their high efficiency and continuously optimizing their properties as a solar cell material. In this Letter, we calculate the shift current response of MAPbI and MAPbICl and show that their current responses are approximately 3 times larger than that of BiFeO_3 . Our calculations demonstrate that the molecular orientations as well as the Cl substitution position can strongly affect their shift current responses.

As shown in ref 22, the short-circuit shift current response σ is a rank three tensor, and it can be computed using perturbation theory, yielding the formula in the thin sample limit as

Received: October 3, 2014

Accepted: November 25, 2014

$$\begin{aligned}
 J_q &= \sigma_{rsq} E_r E_s \\
 \sigma_{rsq}(\omega) &= \pi e \left(\frac{e}{m \hbar \omega} \right)^2 \sum_{n', n''} \int d\mathbf{k} (f[n''\mathbf{k}] - f[n'\mathbf{k}]) \\
 &\times \langle n' \mathbf{k} | \hat{p}_i | n'' \mathbf{k} \rangle \langle n'' \mathbf{k} | \hat{p}_j | n' \mathbf{k} \rangle \\
 &\times \left(-\frac{\partial \phi_{n', n''}(\mathbf{k}, \mathbf{k})}{\partial k_q} - [\chi_{n'' q}(\mathbf{k}) - \chi_{n' q}(\mathbf{k})] \right) \\
 &\times \delta(\omega_{n''}(\mathbf{k}) - \omega_{n'}(\mathbf{k}) \pm \omega)
 \end{aligned} \quad (1)$$

where n and \mathbf{k} are, respectively, the band index and wave vector, f is the occupation, $\hbar\omega_n$ is the energy of state n , $\phi_{n', n''}$ is the phase of the momentum matrix element between state n' and n'' , and χ_n is the Berry connection for state n . If spin-orbit coupling (SOC) is considered, each Bloch state has spinor form, and the current response becomes a sum over spinor components. In a thick sample, considering the light absorption coefficient $\alpha_{rr}(\omega)$, the current response can be described by the Glass coefficient G^{31}

$$G_{rrq} = \frac{\sigma_{rrq}}{\alpha_{rr}} \quad (2)$$

When measuring in-plane current, the total current \mathbf{J} is $J_q(\omega) = G_{rrq} I_r w$, where I is the light intensity and w is the sample width.

The plane wave density functional theory (DFT) package QUANTUM-ESPRESSO³² was used with the generalized gradient approximation (GGA) functional to perform structure relaxations and electronic structure calculations. Norm-conserving, designed nonlocal pseudopotentials were generated with the OPIUM package.^{33,34} A plane wave cutoff energy of 50 Ry was sufficient to converge the total energy. All of the structures were fully relaxed with a force tolerance of 0.005 eV/Å. In order to compute the shift current and Glass coefficient response tensors as shown in eq 1, a self-consistent calculation with a $6 \times 6 \times 4$ k -point grid was performed to find the converged charge density. Then, a non-self-consistent calculation with a much denser k -point grid was performed as needed to converge the shift current response. Due to the presence of heavy atoms, SOC is thought to affect the electronic structure and, by extension, the shift current.^{35,36,50} When SOC is included, an angular-momentum-dependent term is added to the Hamiltonian. In this work, Hamiltonians without SOC (NSOC) and with SOC are considered for electronic structure and shift current calculations, as prediction of a correct band gap is important for shift current calculations.

MAPbI has perovskite-type structure with methylammonium (MA) at the A site and Pb at the B site. The orthorhombic structure is favored at low temperature, but with increasing temperature, it transforms to the tetragonal phase with the $I4/mcm$ space group.^{11,37} The increased symmetry at high temperature is related to the free rotation of the MA molecules, as observed in both experiments and theoretical calculations.^{12,37–41} In order to explore the effect of molecular orientation on the structure and shift current, structures with two different orientations, M1 and M2, starting from the tetragonal PbI_3 inorganic frame, are computed and shown in Figure 1. SOC is found to have a very limited effect on the atomic structure as only the

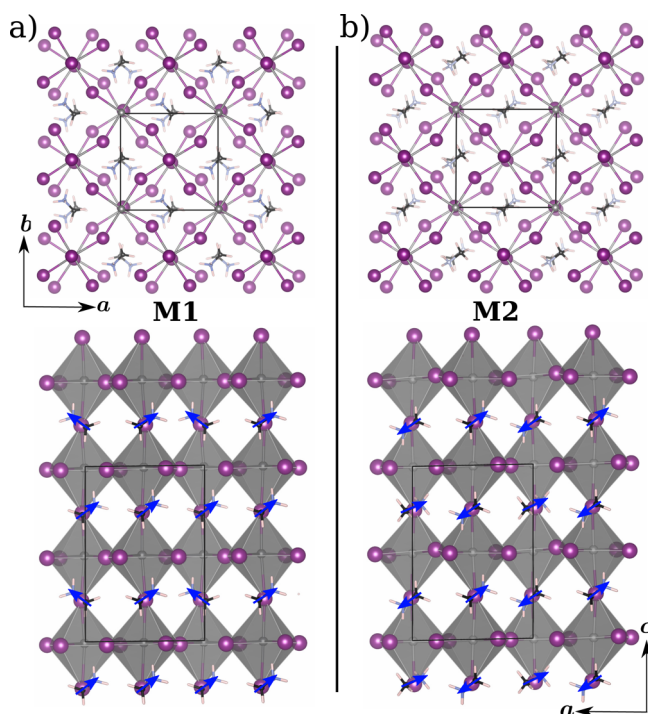


Figure 1. Top and side views of the relaxed MAPbI structures with (a) molecular orientation 1 (M1) and (b) molecular orientation 2 (M2). M1 has all of the net MA molecular dipoles along the c axis, while M2 has MA molecules with dipoles opposite to that of its neighboring molecules, yielding a net-zero dipole. Four MAPbI_3 are considered in one unit cell. Pb: dark gray; I: purple; C: black; N: light blue; Cl: green; H: light pink.

conduction bands that arise mainly from the Pb p orbitals are significantly affected. SOC does not substantially affect the calculation of the ground-state properties, for example, forces.^{7,35,44} Therefore, in the following, we use the atomic structures that are fully relaxed without SOC. The lattice constants of the relaxed structures, as well as the experimental lattice constants, are shown in Table 1. As shown in the table,

Table 1. Lattice Constants and Relative Total Energies, Per Unit Cell, Of the Optimized MAPbI Structures with Molecular Orientation M1 and Molecular Orientation M2^a

	M1	M2	expt.
a (Å)	8.97	9.00	8.85
b (Å)	8.86	8.77	8.85
c (Å)	12.85	12.95	12.44–12.66
E_T (eV)	0.021	0	—

^aThe experimental values are from refs 11, 37, and 42. The total energy (per 48 atom cell) of the M2 orientation structure is set to zero.

our calculated lattice constants agree well with the experiments and theoretical works.^{7,19,35,41,43,44} The computed a and b lattice constants are slightly different depending on the molecular orientations, and because they are different, this confirms that the orthorhombic structure is favored at low temperature. Although the molecular orientations affect the lattice, the total energy difference between the M1 and M2 structures is small.

Figure 2a shows the band structures without and with SOC. As seen in the figure, SOC reduces the band gap substantially

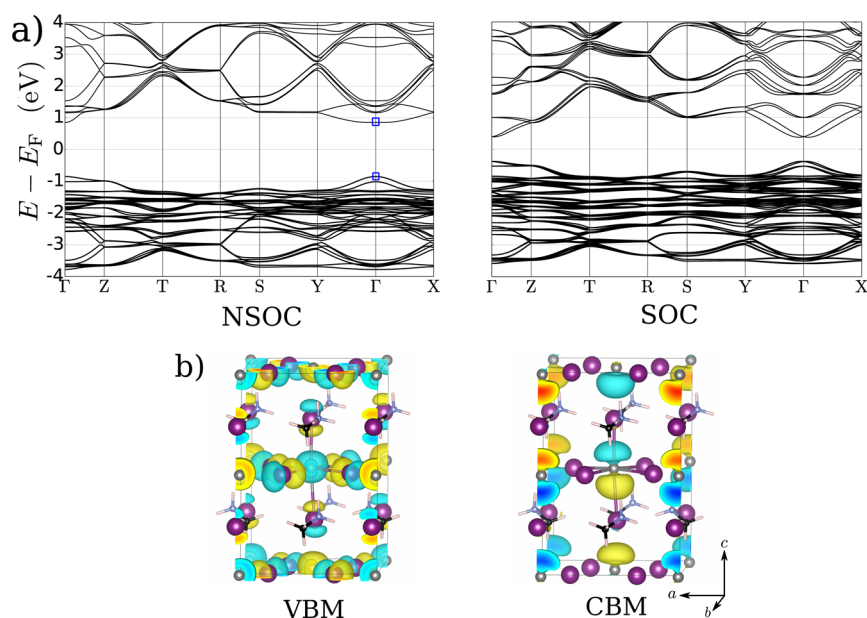


Figure 2. (a) The band structures of MAPbI (M1) without and with SOC. Because the system lacks inversion symmetry, the SOC splits bands that are originally degenerate without SOC. (b) The wave functions of the VBM and CBM at the Γ point without SOC (VBM and CBM states are indicated as blue squares in the NSOC band structure).

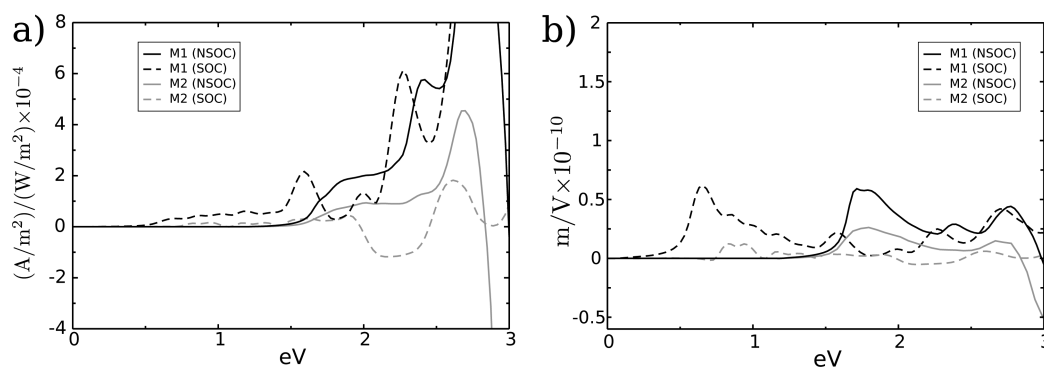


Figure 3. (a) Shift current response σ_{zz} and (b) Glass coefficient G_{zz} versus incident photon energy for structures with molecular orientation M1 and orientation M2. The M1 structure provides a larger shift current response and Glass coefficient than the M2 structure. Calculations with and without SOC show the same trend for the two orientations.

at the Γ point. At this point, the GGA band gap without SOC is close to the experimental value as the DFT underestimation of band gap is largely canceled by the exclusion of SOC. This has been seen in GW and hybrid functional calculations.^{7,14} Our calculated electronic structure (NSOC) shows that the conduction band minimum (CBM) has mostly nonbonding Pb p_z orbital character slightly hybridized with I s , whereas the valence band maximum (VBM) is antibonding between I p and Pb s orbitals, as shown by the real space wave function plots in Figure 2b. The MA molecular electronic states are not directly involved in the states near the band gap, as confirmed by other first-principles calculations.^{15,39}

Because the zzZ response tensor component is the dominant component among all of the tensor elements, Figure 3 shows the MAPbI thin sample limit shift current response σ_{zz} and Glass coefficient response G_{zz} for the M1 and M2 structures with and without SOC. Because the direct band gap calculated with SOC is smaller than that without SOC, the onset energy of the shift current response calculated with SOC is lower than that calculated without SOC, as shown in Figure 3. Also, the SOC tends to shift the whole

spectrum without substantially changing its magnitude. On average, the M2 structure has a much smaller current response and Glass coefficient than the M1 structure. The magnitude of the Glass coefficient is closely related to material symmetry and state delocalization.²² We have shown that a strongly distorted structure with delocalized states involved in an optical transition tends to give a large Glass coefficient response. Polarization calculations show that the M1 structure has a polarization of $5 \mu\text{C}/\text{cm}^2$, while the M2 structure has nearly zero polarization. Because the bulk polarization contribution from the molecular dipole moment is estimated to be less than $2.5 \mu\text{C}/\text{cm}^2$,^{45–47} the PbI_3 inorganic lattice is a significant contributor to the M1 structure's polarization as much larger Pb displacement ($\approx 0.07 \text{ \AA}$ along z) was observed than in the M2 structure ($\approx 0.01 \text{ \AA}$ along z). As a result, the distorted M1 structure provides a larger shift current response than the more symmetric M2 structure. At room temperature, the shift current responses can be the average of the M1 and M2 cases due to the disordered molecular orientations. Limiting the molecular rotation by methods such as doping, lattice

shrinkage, or application of electric field can highlight the current contribution from one particular orientation. An understanding of the dependence of the current on molecular and polarization orientations is helpful in understanding the I/V hysteresis under different applied voltage scanning rates.

Adding Cl has been shown to provide a diffusion length as long as $1\ \mu\text{m}$ without substantially changing the absorption spectrum.^{4,13,15} Because MAPbCl has been found to have a reduced lattice constant along the c axis compared to MAPbI, it is thought that Cl substitutes I at the apical site of the PbI_6 octahedra, but the actual Cl position is still not clear.^{48,49} In order to understand the effects of Cl position on shift current, we study different Cl substitution configurations at the apical and equatorial sites for both molecular orientations, as shown in Figure 4.

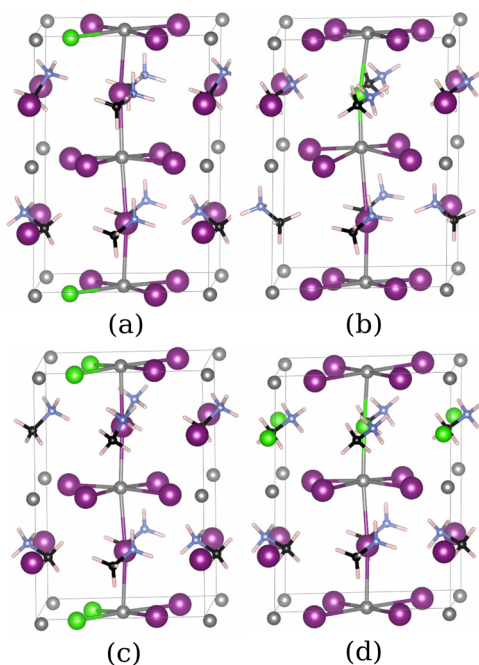


Figure 4. Fully relaxed structures of MAPbCl with one (a,b) or two (c,d) Cl atoms per unit cell. The structures shown here have molecular orientation M1. Structures a and c have equatorial site substitution; structures b and d have apical substitution. The corresponding four structures with molecular orientation M2 are also tested but are not shown here.

The structures with one and two Cl atoms in one unit cell (with 48 atoms) are fully relaxed, and their band gaps and polarization magnitudes are shown in Table 2. The structures with Cl at different positions have similar total energies (≈ 30

meV of the total energy difference), indicating their similar thermal stabilities. We find that although the Cl position has no substantial effect on the polarization, it strongly affects the shift current responses. Figure 5 shows the Glass coefficient G_{zzz} . Responses with and without SOC show a similar trend for different Cl positions and concentrations. Interestingly, the apical site substitution of I with Cl tends to give relatively small shift current responses, while the equatorial site substitution shows much larger responses. This can be explained from wave function projections. Our electronic structure calculations show that Pb p orbital character slightly hybridized with I dominates the conduction bands near the band gap. In the highly symmetric structure without octahedral tilting, Pb p_x , p_y , and p_z will be degenerate and hybridized with I s . However, the distortion of Pb–I bonds on the a – b plane will cause the Pb p orbitals to hybridize with I p orbitals in addition to I s orbitals. This will lift the original degeneracy between $p_{x/y}$ and p_z , allowing Pb p_z to become the dominant orbital character of the CBM. This is very clear in the NSOC case. Wave functions calculated with SOC show a similar picture, but it is not as obvious as in the NSOC case because orbitals with different angular momentum are mixed together. We can see from the projected density of states (PDOS) calculated without SOC (Figure 6) that for the structure without Cl, the CBM has mostly Pb p_z orbital character. With increasing Cl concentration at the apical site, the strong electronegativity of Cl increases the energy bands with Pb p_z orbital character while leaving $p_{x/y}$ unchanged, allowing for a larger band gap. The CBM state, mainly composed of hybridized $p_{x/y}$ orbital character, reduces the current flowing along the z direction because the $p_{x/y}$ orbitals are less delocalized than p_z orbitals along z . However, the Cl concentration only moderately affects the shift current response as structures containing one Cl atom yield responses similar in magnitude to those of structures containing two Cl atoms.

The shift current is also calculated for the molecular orientation M2, which has the same Cl configurations discussed previously. Overall, their responses, shown in Figure 7, are smaller than that corresponding to the M1 orientation and are similar to the case without Cl. The minor electronic contribution of the organic species at the band edge, evident from the PDOS, suggests that the effect of the molecular orientation on the shift current is likely indirect, occurring through the PbI_3 frame. In this case, because the molecular dipoles for the neighboring molecules are opposite, there is no net dipolar effect on the PbI_3 frame, resulting in a nearly symmetric frame. As the distortion decreases, the dependence of current response on different Cl positions becomes less significant, as in the M1 case.

Table 2. Total Polarization Magnitude ($|P|$), the z Component ($|P_z|$), and the Band Gap for MAPbI and MAPbCl Structures (a–d in Figure 4) with Both Molecular Orientations (M1 and M2)

structure	M1				M2			
	$ P $ ($\mu\text{C}/\text{cm}^2$)	$ P_z $ ($\mu\text{C}/\text{cm}^2$)	band gap (eV)		$ P $ ($\mu\text{C}/\text{cm}^2$)	$ P_z $ ($\mu\text{C}/\text{cm}^2$)	band gap (eV)	
			NSOC	SOC			NSOC	SOC
MAPbI	6.8	5.0	1.72	0.69	0.7	0.5	1.70	0.75
a	8.3	7.2	1.75	0.76	1.8	1.0	1.72	0.80
b	8.0	6.3	1.90	0.83	2.6	2.4	1.84	0.83
c	6.9	6.2	1.93	0.83	2.3	0.3	1.93	0.83
d	6.1	4.4	1.96	0.84	3.3	3.2	1.91	0.83

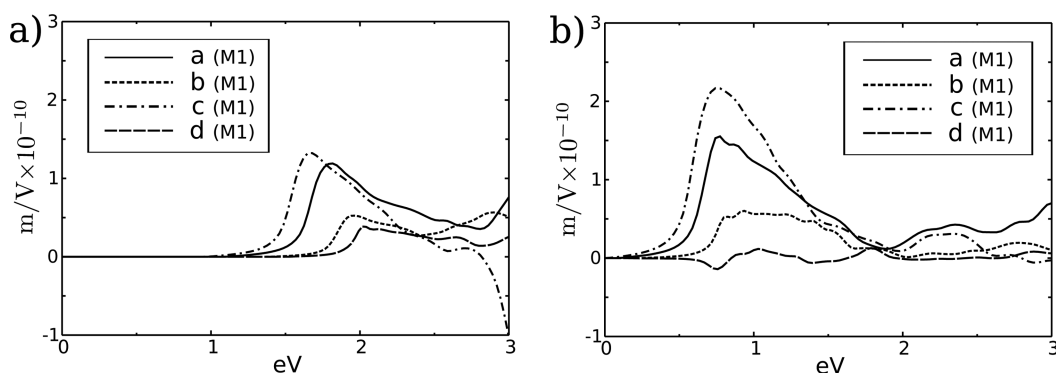


Figure 5. Glass coefficient G_{zzZ} calculated with (a) NSOC and (b) SOC versus incident photon energy for the four relaxed structures (a–d) shown in Figure 4

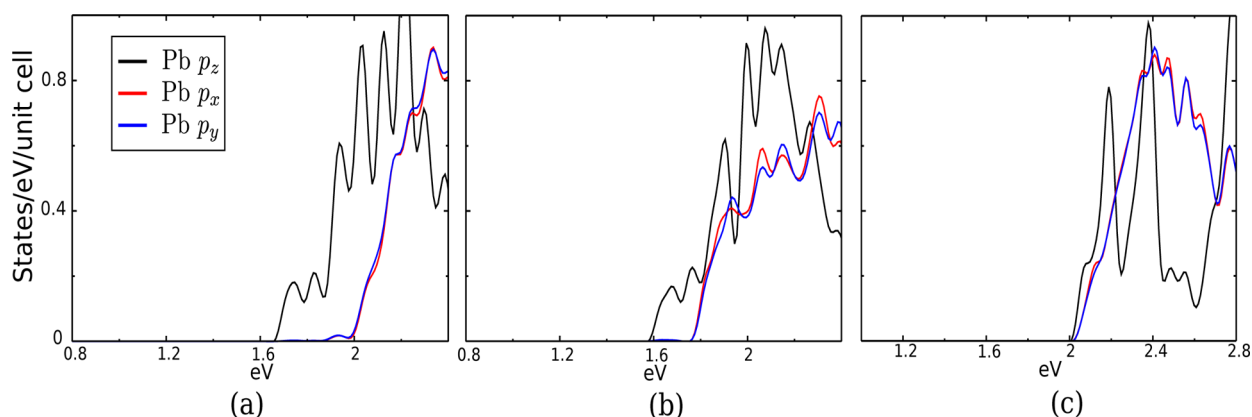


Figure 6. PDOS for Pb atoms calculated from structure (a) M1 orientation without Cl in Figure 1, (b) structure c(M1), and (c) d(M1) in Figure 4. The energy of the VBM is set to zero.

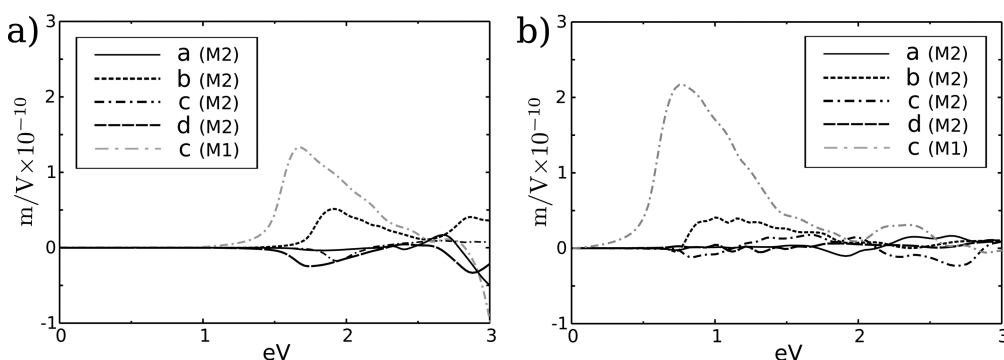


Figure 7. Glass coefficient G_{zzZ} for (a) NSOC and (b) SOC for the four relaxed structures (a–d) shown in Figure 4 but with molecular orientation M2. For comparison, the largest response from the M1 case (structure c(M1)) is also plotted as a gray line. On average, the M2 orientation gives smaller responses than the M1 orientation for the four structures.

In summary, we calculate the shift current responses and polarization magnitudes of MAPbI and MAPbICl from first-principles with and without SOC. We find that the SOC does not substantially alter the spectrum, though it reduces the band gap. Rather, the MA orientation and Cl substitution position can strongly affect the shift current response. When the MA molecules' net dipole moments are aligned in parallel, the PbI₃ inorganic frame becomes more distorted, resulting in relatively large shift current responses. Conversely, when the molecules have opposite dipole moments, the structure is nearly symmetric, resulting in much smaller shift current responses. The substitution of Cl at the equatorial site can enhance the shift current response because the orbital

character contribution at the CBM is more delocalized along the shift current direction. Thus, a higher shift current response can be obtained by introducing a large lattice distortion with MA molecules aligned in parallel and by substituting Cl at equatorial positions.

AUTHOR INFORMATION

Corresponding Author

*E-mail: rappe@sas.upenn.edu.

Notes

The authors declare no competing financial interest.

ACKNOWLEDGMENTS

F.Z. was supported by the Department of Energy Office of Basic Energy Sciences under Grant Number DE-FG02-07ER46431. H.T. was supported by the Office of Naval Research under Grant Number N00014-12-1-1033. F.W. was supported by the Department of Energy Office of Basic Energy Sciences under Grant Number DE-FG02-07ER46431. N.Z.K. was supported by Office of Naval Research under Grant Number N00014-14-1-0761 and by the Roy & Diana Vagelos Scholars Program in the Molecular Life Sciences. A.M.R. was supported by the National Science Foundation under Grant Number CMMI-1334241. Computational support was provided by the High-Performance Computing Modernization Office of the Department of Defense and the National Energy Research Scientific Computing Center.

REFERENCES

- (1) Kim, H.-S.; Lee, C.-R.; Im, J.-H.; Lee, K.-B.; Moehl, T.; Marchioro, A.; Moon, S.-J.; Humphry-Baker, R.; Yum, J.-H.; Moser, J. E.; et al. Lead iodide perovskite sensitized all-solid-state submicron thin film mesoscopic solar cell with efficiency exceeding 9%. *Sci. Rep.* **2012**, *2*, 591.
- (2) Zhou, H.; Chen, Q.; Li, G.; Luo, S.; Song, T.-b.; Duan, H.-S.; Hong, Z.; You, J.; Liu, Y.; Yang, Y. Interface engineering of highly efficient perovskite solar cells. *Science* **2014**, *345*, 542–546.
- (3) Gao, P.; Nazeeruddin, M. K.; Grätzel, M. Organohalide lead perovskites for photovoltaic applications. *Energy Environ. Sci.* **2014**, *7*, 2448–2463.
- (4) Stranks, S. D.; Eperon, G. E.; Grancini, G.; Menelaou, C.; Alcocer, M. J.; Leijtens, T.; Herz, L. M.; Petrozza, A.; Snaith, H. J. Electron–hole diffusion lengths exceeding 1 micrometer in an organometal trihalide perovskite absorber. *Science* **2013**, *342*, 341–344.
- (5) Papavassiliou, G. C.; Koutselas, I. Structural, optical and related properties of some natural three- and lower-dimensional semiconductor systems. *Synth. Met.* **1995**, *71*, 1713–1714.
- (6) Noel, N. K.; Stranks, S. D.; Abate, A.; Wehrenfennig, C.; Guarnera, S.; Haghighirad, A.; Sadhanala, A.; Eperon, G. E.; Pathak, S. K.; Johnston, M. B.; et al. Lead-free organic–inorganic tin halide perovskites for photovoltaic applications. *Energy Environ. Sci.* **2014**, *7*, 3061–3068.
- (7) Umari, P.; Mosconi, E.; De Angelis, F. Relativistic GW calculations on $\text{CH}_3\text{NH}_3\text{PbI}_3$ and $\text{CH}_3\text{NH}_3\text{SnI}_3$ perovskites for solar cell applications. *Sci. Rep.* **2014**, *4*, 4467.
- (8) Chiarella, F.; Zappettini, A.; Licci, F.; Borriello, I.; Cantele, G.; Ninno, D.; Cassinese, A.; Vaglio, R. Combined experimental and theoretical investigation of optical, structural, and electronic properties of $\text{CH}_3\text{NH}_3\text{SnX}_3$ thin films (X = Cl, Br). *Phys. Rev. B* **2008**, *77*, 045129.
- (9) Ogomi, Y.; Morita, A.; Tsukamoto, S.; Saitho, T.; Fujikawa, N.; Shen, Q.; Toyoda, T.; Yoshino, K.; Pandey, S. S.; Ma, T.; et al. $\text{CH}_3\text{NH}_3\text{Sn}_{1-x}\text{Pb}_x\text{I}_3$ perovskite solar cells covering up to 1060 nm. *J. Phys. Chem. Lett.* **2014**, *5*, 1004–1011.
- (10) Eperon, G. E.; Stranks, S. D.; Menelaou, C.; Johnston, M. B.; Herz, L. M.; Snaith, H. J. Formamidinium lead trihalide: a broadly tunable perovskite for efficient planar heterojunction solar cells. *Energy Environ. Sci.* **2014**, *7*, 982–988.
- (11) Stoumpos, C. C.; Malliakas, C. D.; Kanatzidis, M. G. Semiconducting tin and lead iodide perovskites with organic cations: phase transitions, high mobilities, and near-infrared photoluminescent properties. *Inorg. Chem.* **2013**, *52*, 9019–9038.
- (12) Mosconi, E.; Quarti, C.; Ivanovska, T.; Ruani, G.; De Angelis, F. Structural and electronic properties of organo-halide lead perovskites: a combined IR-spectroscopy and ab initio molecular dynamics investigation. *Phys. Chem. Chem. Phys.* **2014**, *16*, 16137–16144.
- (13) Green, M. A.; Ho-Baillie, A.; Snaith, H. J. The emergence of perovskite solar cells. *Nat. Photonics* **2014**, *8*, 506–514.
- (14) Feng, J.; Xiao, B. Crystal structures, optical properties, and effective mass tensors of $\text{CH}_3\text{NH}_3\text{PbX}_3$ (X=I and Br) phases predicted from HSE06. *J. Phys. Chem. Lett.* **2014**, *5*, 1278–1282.
- (15) Filippetti, A.; Mattoni, A. Hybrid perovskites for photovoltaics: insights from first principles. *Phys. Rev. B* **2014**, *89*, 125203.
- (16) Ponseca, J.; Carlito, S.; Savenije, T. J.; Abdellah, M.; Zheng, K.; Yartsev, A.; Pascher, T.; Harlang, T.; Chabera, P.; Pullerits, T.; Stepanov, A.; et al. Organometal halide perovskite solar cell materials rationalized: ultrafast charge generation, high and microsecond-long balanced mobilities, and slow recombination. *J. Am. Chem. Soc.* **2014**, *136*, 5189–5192.
- (17) Xing, G.; Mathews, N.; Sun, S.; Lim, S. S.; Lam, Y. M.; Graetzel, M.; Mhaisalkar, S.; Sum, T. C. Long-range balanced electron- and hole-transport lengths in organic-inorganic $\text{CH}_3\text{NH}_3\text{PbI}_3$. *Science* **2013**, *342*, 344–347.
- (18) Edri, E.; Kirmayer, S.; Mukhopadhyay, S.; Gartsman, K.; Hodes, G.; Cahen, D. Elucidating the charge carrier separation and working mechanism of $\text{CH}_3\text{NH}_3\text{PbI}_{3-x}\text{Cl}_x$ perovskite solar cells. *Nat. Commun.* **2014**, *5*, 3461.
- (19) Kim, J.; Lee, S.-H.; Lee, J. H.; Hong, K.-H. The role of intrinsic defects in methylammonium lead iodide perovskite. *J. Phys. Chem. Lett.* **2014**, *5*, 1312–1317.
- (20) Yin, W.-J.; Shi, T.; Yan, Y. Unusual defect physics in $\text{CH}_3\text{NH}_3\text{PbI}_3$ perovskite solar cell absorber. *Appl. Phys. Lett.* **2014**, *104*, 063903.
- (21) Du, M. H. Efficient carrier transport in halide perovskites: theoretical perspectives. *J. Mater. Chem. A* **2014**, *2*, 9091–9098.
- (22) Young, S. M.; Rappe, A. M. First principles calculation of the shift current photovoltaic effect in ferroelectrics. *Phys. Rev. Lett.* **2012**, *109*, 116601.
- (23) Young, S. M.; Zheng, F.; Rappe, A. M. First-principles calculation of the bulk photovoltaic effect in bismuth ferrite. *Phys. Rev. Lett.* **2012**, *109*, 236601.
- (24) Sipe, J. E.; Shkrebtii, A. I. Second-order optical response in semiconductors. *Phys. Rev. B* **2000**, *61*, 5337–5352.
- (25) von Baltz, R.; Kraut, W. Theory of the bulk photovoltaic effect in pure crystals. *Phys. Rev. B* **1981**, *23*, 5590–5596.
- (26) Snaith, H. J.; Abate, A.; Ball, J. M.; Eperon, G. E.; Leijtens, T.; Noel, N. K.; Stranks, S. D.; Wang, J. T.-W.; Wojciechowski, K.; Zhang, W. Anomalous hysteresis in perovskite solar cells. *J. Phys. Chem. Lett.* **2014**, *5*, 1511–1515.
- (27) Sánchez, R. S.; Gonzalez-Pedro, V.; Lee, J.-W.; Park, N.-G.; Kang, Y. S.; Mora-Sero, I.; Bisquert, J. Slow dynamic processes in lead halide perovskite solar cells. characteristic times and hysteresis. *J. Phys. Chem. Lett.* **2014**, *5*, 2357.
- (28) Dualeh, A.; Moehl, T.; Tétreault, N.; Teuscher, J.; Gao, P.; Nazeeruddin, M. K.; Grätzel, M. Impedance spectroscopic analysis of lead iodide perovskite-sensitized solid-state solar cells. *ACS Nano* **2013**, *8*, 362–373.
- (29) Docampo, P.; Hanusch, F. C.; Giesbrecht, N.; Angloher, P.; Ivanova, A.; Bein, T. Influence of the orientation of methylammonium lead iodide perovskite crystals on solar cell performance. *APL Mater.* **2014**, *2*, 081508.
- (30) Jeon, N. J.; Noh, J. H.; Kim, Y. C.; Yang, W. S.; Ryu, S.; Seok, S. I. Solvent engineering for high-performance inorganic–organic hybrid perovskite solar cells. *Nat. Mater.* **2014**, *13*, 897–903.
- (31) Glass, A. M.; von der Linde, D.; Negran, T. J. High-voltage bulk photovoltaic effect and photorefractive process in LiNbO_3 . *Appl. Phys. Lett.* **1974**, *25*, 233–235.
- (32) Giannozzi, P.; Baroni, S.; Bonini, N.; Calandra, M.; Car, R.; Cavazzoni, C.; Ceresoli, D.; Chiarotti, G. L.; Cococcioni, M.; Dabo, I.; et al. Quantum ESPRESSO: a modular and open-source software project for quantum simulations of materials. *J. Phys.: Condens. Matter* **2009**, *21*, 395502–395520.
- (33) Rappe, A. M.; Rabe, K. M.; Kaxiras, E.; Joannopoulos, J. D. Optimized pseudopotentials. *Phys. Rev. B* **1990**, *41*, 1227–1230.

- (34) Ramer, N. J.; Rappe, A. M. Designed nonlocal pseudopotentials for enhanced transferability. *Phys. Rev. B* **1999**, *59*, 12471–12478.
- (35) Amat, A.; Mosconi, E.; Ronca, E.; Quarti, C.; Umari, P.; Nazeeruddin, M. K.; Graetzel, M.; De Angelis, F. Cation-induced band-gap tuning in organohalide perovskites: interplay of spin–orbit coupling and octahedra tilting. *Nano Lett.* **2014**, *14*, 3608–3616.
- (36) Even, J.; Pedesseau, L.; Jancu, J.-M.; Katan, C. Importance of spin–orbit coupling in hybrid organic/inorganic perovskites for photovoltaic applications. *J. Phys. Chem. Lett.* **2013**, *4*, 2999–3005.
- (37) Poglitsch, A.; Weber, D. Dynamic disorder in methylammoniumtrihalogenoplumbates (II) observed by millimeter-wave spectroscopy. *J. Chem. Phys.* **1987**, *87*, 6373–6378.
- (38) Quarti, C.; Grancini, G.; Mosconi, E.; Bruno, P.; Ball, J. M.; Lee, M. M.; Snaith, H. J.; Petrozza, A.; Angelis, F. D. The Raman spectrum of the $\text{CH}_3\text{NH}_3\text{PbI}_3$ hybrid perovskite: interplay of theory and experiment. *J. Phys. Chem. Lett.* **2013**, *5*, 279–284.
- (39) Frost, J. M.; Butler, K. T.; Brivio, F.; Hendon, C. H.; van Schilfgaarde, M.; Walsh, A. Atomistic origins of high-performance in hybrid halide perovskite solar cells. *Nano Lett.* **2014**, *14*, 2584–2590.
- (40) Brivio, F.; Walker, A. B.; Walsh, A. Structural and electronic properties of hybrid perovskites for high-efficiency thin-film photovoltaics from first-principles. *APL Mater.* **2013**, *1*, 042111.
- (41) Wang, Y.; Gould, T.; Dobson, J. F.; Zhang, H.; Yang, H.; Yao, X.; Zhao, H. Density functional theory analysis of structural and electronic properties of orthorhombic perovskite $\text{CH}_3\text{NH}_3\text{PbI}_3$. *Phys. Chem. Chem. Phys.* **2014**, *16*, 1424–1429.
- (42) Baikie, T.; Fang, Y.; Kadro, J. M.; Schreyer, M.; Wei, F.; Mhaisalkar, S. G.; Graetzel, M.; White, T. J. Synthesis and crystal chemistry of the hybrid perovskite $(\text{CH}_3\text{NH}_3)\text{PbI}_3$ for solid-state sensitised solar cell applications. *J. Mater. Chem. A* **2013**, *1*, 5628–5641.
- (43) Mosconi, E.; Amat, A.; Nazeeruddin, M. K.; Graetzel, M.; De Angelis, F. First-principles modeling of mixed halide organometal perovskites for photovoltaic applications. *J. Phys. Chem. C* **2013**, *117*, 13902–13913.
- (44) Egger, D. A.; Kronik, L. Role of dispersive interactions in determining structural properties of organic–inorganic halide perovskites: insights from first-principles calculations. *J. Phys. Chem. Lett.* **2014**, *5*, 2728–2733.
- (45) The dipole moment of molecule CH_3NH_3^+ is calculated as 2.2 D with HF/6-311G(p,d) using GAMESS.
- (46) Dykstra, C.; Frenking, G.; Kim, K.; Scuseria, G. *Theory and applications of computational chemistry: the first forty years*; Elsevier: New York, 2011.
- (47) Schmidt, M. W.; Baldridge, K. K.; Boatz, J. A.; Elbert, S. T.; Gordon, M. S.; Jensen, J. H.; Koseki, S.; Matsunaga, N.; Nguyen, K. A.; Su, S. J.; et al. General atomic and molecular electronic structure system. *J. Comput. Chem.* **1993**, *14*, 1347–1363.
- (48) Lee, M. M.; Teuscher, J.; Miyasaka, T.; Murakami, T. N.; Snaith, H. J. Efficient hybrid solar cells based on meso-superstructured organometal halide perovskites. *Science* **2012**, *338*, 643–647.
- (49) Colella, S.; Mosconi, E.; Pellegrino, G.; Alberti, A.; Guerra, V. L.; Masi, S.; Listorti, A.; Rizzo, A.; Condorelli, G. G.; De Angelis, F.; et al. The elusive presence of chloride in mixed halide perovskite solar cells. *J. Phys. Chem. Lett.* **2014**, *5*, 3532–3538.
- (50) Stroppa, A.; Barone, P.; Jain, P.; Perez-Mato, J.; Picozzi, S. Hybrid improper ferroelectricity in a multiferroic and magnetoelectric metal–organic framework. *Adv. Mater.* **2013**, *25*, 2284–2290.